Impact of underwater-ice evolution on Arctic summer sea ice

Dirk Notz,[1,4] Miles G. McPhee,[2] M. Grae Worster,[1] Gary A. Maykut,[3]
K. Heinke Schlünzen,[5] and Hajo Eicken[6]

Received 12 October 2001; revised 12 June 2002; accepted 8 August 2002; published 10 July 2003.

[1] A model is presented that describes the simultaneous growth and ablation of a layer of ice between an under-ice melt pond and the underlying ocean. Such "false bottoms" are the only significant source of ice formation in the Arctic during summer. Analytical solutions for diffusional transport of heat and salt are calculated that illustrate the importance of salt transport in effecting phase change. The model is extended to account for turbulent transports and applied to make predictions of bottom ablation rates of sea ice given the far-field properties of the ocean from the AIDJEX and SHEBA field experiments. The model predictions show that false bottoms may play a significant role in the summer heat budget of the ice-ocean system, causing localized heat fluxes of more than 10 W m^{-2} into the mixed layer. The thickening of thin ice by false-bottom formation leads to longer-lasting sea ice and thus smaller ice-free areas, which might be an important mechanism affecting the surface albedo. *INDEX TERMS:* 4207 Oceanography: General: Arctic and Antarctic oceanography; 4540 Oceanography: Physical: Ice mechanics and air/sea/ice exchange processes; 4524 Oceanography: Physical: Fine structure and microstructure; *KEYWORDS:* sea ice, heat fluxes, mushy layer, melt pond, turbulent fluxes

Citation: Notz, D., M. G. McPhee, M. G. Worster, G. A. Maykut, K. H. Schlünzen, and H. Eicken, Impact of underwater-ice evolution on Arctic summer sea ice, *J. Geophys. Res.*, *108*(C7), 3223, doi:10.1029/2001JC001173, 2003.

1. Introduction

[2] Sea ice interacts both dynamically and thermodynamically with the atmosphere and the ocean. During the summer, when the air temperature is above 0°C, these interactions cause ablation to occur at both the surface and the bottom of the ice. Whereas surface ablation is dominant for the thinning and shrinking of the Arctic sea ice cover during summer, nearly all the ablation in the Antarctic takes place at the bottom [*Andreas and Ackley*, 1982; *Maykut*, 1985]. As described by *Untersteiner* [1968] and *Eicken et al.* [2002], the meltwater in the Arctic can be diverted into three different reservoirs. First, meltwater collects in surface melt ponds, which is the most important reservoir. Second, meltwater can percolate into the ice matrix, leading to a strong reduction in the surface salinities of Arctic sea ice [*Untersteiner*, 1968]. Third, meltwater gets discharged under the ice through highly permeable ice or flaws and along floe margins. This meltwater can be retained under thin ice or in bottom depressions, leading to fresh water lenses which *Hanson* [1965] calls "under-ice melt ponds." At the interface between this (light) fresh water and the underlying (dense) salt water, double-diffusive convection of heat and salt occurs, leading to the formation of underwater ice, called false bottoms [*Untersteiner and Badgley*, 1958; *Hanson*, 1965; *Martin and Kauffman*, 1974; *Cherepanov et al.*, 1989; *Eicken*, 1994; *Eicken et al.*, 2002]. *Nansen* [1897] noted that this is the only process by which significant amounts of new ice can be formed during the summer. He observed around 0.2 m of summer ice growth due to false bottoms.

[3] False bottoms normally form in under-ice melt ponds, where the fresh water is relatively protected from being mixed into the underlying salt water. Sometimes false bottom formation occurs under cracks and small leads, where the surrounding ice provides the same protection (Figure 1). The properties of false bottoms and under-ice melt ponds are difficult to measure nondestructively because coring under the surface melt ponds, which normally lie above the under-ice melt ponds, would cause direct mixing of under-ice and surface water. Because of this and other sampling problems, the areal extent and overall volume of false bottoms is still not reliably known. Of a set of ice cores collected at 52 locations in the Eurasian Arctic by *Eicken* [1994], eight contained false bottoms as indicated by textural and isotopic analysis. Given an average ice age of 3 years, this suggests that at least 5% of the level ice bottom area is underlain by false bottoms during a given

[1]Institute of Theoretical Geophysics, Department of Applied Mathematics and Theoretical Physics, University of Cambridge, UK.
[2]McPhee Research Company, Naches, Washington, USA.
[3]Department of Atmospheric Sciences, University of Washington, Seattle, Washington, USA.
[4]Formerly at Meteorologisches Institut, Zentrum für Meeres- und Klimaforschung, Universität Hamburg, Germany.
[5]Meteorologisches Institut, Zentrum für Meeres- und Klimaforschung, Universität Hamburg, Germany.
[6]Geophysical Institute, University of Alaska, Fairbanks, Alaska, USA.

0148-0227/03/2001JC001173$09.00

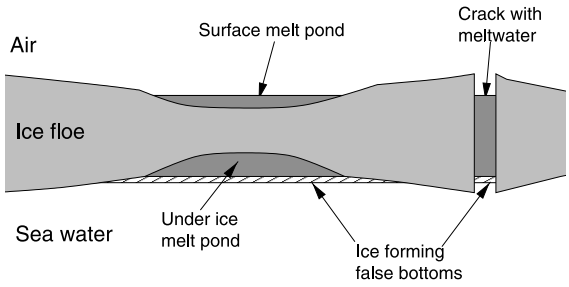

Figure 1. Sketch of an under-ice melt pond, after *Martin and Kauffman* [1974].

summer. *Jeffries et al.* [1995] found traces of false-bottom ice in 22 of 57 cores analyzed in the Beaufort Sea, corresponding to an areal coverage of false bottoms of at least 10% of the level ice for an average ice age of 4 years. *Hanson* [1965] estimated that under-floe melt ponds and false bottoms covered half of the flow bottom of the drifting station "Charlie." This probably represents an upper bound of the areal coverage of false bottoms, and Hanson's measurements may have been affected by artificial drainage in the vicinity of an ice camp. However, as *Jeffries et al.* [1995] point out, the possibility that ice growth in under-ice melt ponds is common and not an oddity is consistent with the interpretation of data obtained by submarine sonar measurements [*Wadhams and Martin*, 1990].

[4] During the field experiment Surface Heat Budget of the Arctic Ocean (SHEBA) [see *Perovich et al.*, 1999], false bottoms seemed to be a fairly common feature [*Eicken et al.*, 2002]. For example, approximately 15% of a total of more than 100 mass-balance gauges distributed over the SHEBA study area in the Northern Chukchi Sea developed false bottoms at some point during the ablation season [*Perovich et al.*, 2003]. The initial formation of false bottoms usually took only a couple of hours. Large crystals were observed, growing laterally from the walls of the under-ice cavity at the interface. This mechanism of initial false-bottom formation is much faster than that in the combined laboratory and theoretical study by *Martin and Kauffman* [1974], which was characterized by purely vertical ice formation. This difference in growth rates is a consequence of the different geometry. Formation of false bottoms at the SHEBA site occurred at such a speed as to trap Arctic cod within the ice cover.

[5] Because meltwater collects mostly in cavities under (relatively) thin ice such as young ice formed in leads, false bottoms normally do not occur under (relatively) thick ice, thus providing a leveling mechanism of the under ice topography (see Figure 1). As false bottoms protect the overlying sea-ice bottom from the ocean heat-flux, the assumption that thin ice (under which false bottoms preferably form) melts more rapidly than thick ice is not valid in general, even though this statement is certainly true for surface melting owing to the differences in albedo.

[6] *Martin and Kauffman* [1974] showed in their experiments that false bottoms slowly migrate upward due to bottom ablation, while simultaneously getting thicker at the top due to freezing of fresh water from the under-ice melt pond above. At several locations during SHEBA, two to four false bottoms were found on top of one another, with fresh water lenses between them. These were formed by fresh water collecting in under-ice concavities beneath false bottoms, leading to formation of a second thin ice layer below the original. On the basis of observations of migration velocities at the field site and in experiments [*Martin and Kauffman*, 1974], closely stacked or enjoined false bottoms are most likely due to merging of a lower ice layer with an upper one that had become stationary once contact with sea water was lost.

[7] The ice formed during the formation of false bottoms can be clearly distinguished from normal sea ice by both its crystal shape and its $\delta^{18}O$ value [*Eicken*, 1994]. As *Eicken et al.* [2002] measured at the SHEBA camp during summer 1998, at the end of the melting period the water in the under-ice melt ponds had the highest percental amount of meteoric water (i.e., snow meltwater) among all meltwater reservoirs. Thus false bottoms may play an important role in the transfer of pollutants from the atmosphere into the ice pack, which could lead to an accumulation of pollutants at the biologically important ice underside [*Gradinger*, 1996].

[8] Since false bottoms consist of nearly fresh ice (during SHEBA $S < 1$ psu), the underlying ocean water is at a temperature below the melting point of the ice. This is also true for the rest of the sea ice pack, meaning the bottom of sea ice does not melt per se but rather dissolves into the relatively salty ocean; that is, the change of phase requires the transport of salt to the phase boundary and cannot occur by purely thermal processes. In section 2 of this study we present the theoretical background of the processes leading to bottom ablation of sea ice and to the formation of false bottoms. The governing equations are solved for the case of pure ice, corresponding to a false bottom, and the implications of the model for general sea ice are discussed. In section 3 the model is adjusted to ocean conditions by including turbulent heat and salt fluxes, allowing the prediction of bottom ablation rates and false bottom evolution for given far-field properties. Section 4 presents a comparison of model results with laboratory and field experiments. More details are given by *Notz* [2001].

2. Model of Bottom Ablation and False Bottom Evolution for Nonturbulent Conditions

2.1. Treatment of Bottom Ablation

[9] Ablation of the sea-ice-ocean interface is caused by dissolution rather than by melting. Specifically, since the temperature of the ocean is normally below the melting point of the relatively fresh sea ice, the change of phase from solid to liquid requires the intermixing of salt and water molecules to form a solution, similar to the way in which sugar is dissolved in water, even though the water temperature is far below the melting point of the sugar. Therefore dissolution is rate limited by salt transport whereas melting can proceed at the much higher rates characteristic of heat transport. For further discussion of melting versus dissolution, see *Woods* [1992].

[10] During binary (two-component) solidification and dissolution, two boundary conditions must be fulfilled at the interface between the ice and the water: one for the flux of heat and one for the flux of salt [*Woods*, 1992; *Worster*, 2000]. To illustrate the most important interactions, we formulate a model in which we neglect turbulent transport

and take into account molecular diffusion in the water and heat conduction in the ice. If the ablation rate of the ice is $\dot{h} \equiv \partial h/\partial t$, then the net amount of heat that must be transferred to the interface is $\rho L\dot{h}$, with ρ being the density of the ice and L being the latent heat of fusion. This heat represents the difference of the heat fluxes in the ice and the ocean, which gives the Stefan condition for the heat balance at the interface

$$\rho L\dot{h}(t) = k_i \left.\frac{\partial T}{\partial z}\right|_{\text{ice}} - k_w \left.\frac{\partial T}{\partial z}\right|_{\text{water}}. \tag{1}$$

Here k is thermal conductivity, the subscripts i and w refer, as for the remainder of this paper, to ice and water, T is temperature, and z is the vertical coordinate. The first term on the right-hand side describes the conductive heat flux in the ice at the interface; the second term gives the heat flux in the water at the interface. The water near the interface is a mixture of the relatively fresh ice melt water and sea water, so its salinity is less than the far field salinity. There must be an equilibrium of salt being transported into this layer and freshening of this layer by bottom ablation of the ice, leading to the conservation relationship,

$$(S_0 - S_i)\dot{h}(t) = -D \left.\frac{\partial S}{\partial z}\right|_{\text{water}}. \tag{2}$$

Here S_0 is the salinity of the ocean at the interface, S_i is the bulk salinity of the ice, and D is the molecular diffusivity of salt in sea water. The left-hand side of the equation gives the rate at which the water at the interface freshens, while the right-hand side gives the rate at which salt diffuses into the water near the interface. These equations are essentially identical to those described by *Martin and Kauffman* [1974].

[11] The interface temperature T_0 and salinity S_0 are connected via the freezing-point relationship,

$$T_0 \approx -mS_0, \tag{3}$$

with $m = 0.054$ °C psu^{-1} for the temperature range of interest here. Relation (3) is an approximation for the liquidus temperature, the temperature at which a solution begins to form a solid phase.

[12] Equations (1) to (3) form a closed system in connection with the diffusion equations for heat and salt in the ice and the ocean,

$$\frac{\partial T}{\partial t} = \kappa \frac{\partial^2 T}{\partial z^2} \tag{4}$$

$$\frac{\partial S}{\partial t} = D \frac{\partial^2 S}{\partial z^2}, \tag{5}$$

where $\kappa = k/\rho c_p$ is the thermal diffusivity, and c_p is the specific heat capacity. To keep the analysis simple, we neglect salt fluxes in the ice and heat fluxes from the fresh water above the false bottom and assume a linear temperature profile through the ice. The Stefan condition at the upper surface of the false bottom thus becomes

$$\rho L\dot{h_u} = k_i \frac{T_u - T_0}{h_u - h}, \tag{6}$$

where h_u and T_u are the position and the temperature of the upper interface.

2.2. Analytical Model for a False Bottom

[13] Because there are no external length scales or timescales in the problem, equations (1)–(6) admit a similarity solution in which $T(z, t)$ and $S(z, t)$ are functions only of the similarity variable $\eta = z/(2\sqrt{Dt})$, which is characteristic of diffusion problems in unbounded domains [see *Carslaw and Jaeger*, 1986]. In terms of η the solution can be expressed as

$$h(t) = 2\lambda\sqrt{Dt}, \tag{7}$$

$$h_u(t) = 2\lambda_u\sqrt{Dt}, \tag{8}$$

$$T(\eta) = T_\infty + (T_0 - T_\infty)\frac{erfc(-\epsilon\eta)}{erfc(-\epsilon\lambda)} \quad (\eta < \lambda), \tag{9}$$

$$T(\eta) = T_0 + (T_f - T_0)\frac{\eta - \lambda}{\lambda_u - \lambda} \quad (\lambda_u > \eta > \lambda), \tag{10}$$

$$S(\eta) = S_\infty + (S_0 - S_\infty)\frac{\text{erfc}(-\eta)}{\text{erfc}(-\lambda)} \quad (\eta < \lambda), \tag{11}$$

where $\varepsilon = \sqrt{D/\kappa_w}$, while λ and λ_u are constants to be determined. The complementary error function is defined as $\text{erfc}(x) = 1 - (\frac{2}{\sqrt{\pi}}\int_0^x e^{-u^2}du)$, and is tabulated, for example, by *Abramovitz and Stegun* [1965]. Note that $\dot{h}$ and $\dot{h}_u$ are both proportional to $\sqrt{D/t}$, with λ and λ_u being the proportionality constants in each case. Larger values of λ and λ_u correspond to higher ablation and accretion rates, respectively. Equations (9) and (11) describe the temperature and salinity field in the water whereas equation (10) describes the (linear) temperature field in the false bottom (see Figure 2).

[14] The coefficients λ and λ_u are determined from the coupled equations, derived from equations (1), (2), and (6), respectively,

$$(S_0 - S_i) = \frac{S_0 - S_\infty}{F(-\lambda)}, \tag{12}$$

$$\frac{L}{c_{pw}} = \frac{1}{2}\frac{k_i}{k_w}\frac{1}{\epsilon^2}\frac{T_f - T_0}{\lambda(\lambda_u - \lambda)} - \frac{T_\infty - T_0}{F(-\epsilon\lambda)}, \tag{13}$$

$$\frac{L}{c_{pw}} = \frac{1}{2}\frac{k_i}{k_w}\frac{1}{\epsilon^2}\frac{T_f - T_0}{\lambda_u(\lambda_u - \lambda)} \tag{14}$$

where

$$F(x) = \sqrt{\pi}xe^{x^2}\text{erfc}(x) \tag{15}$$

and c_{pw} is the specific heat of water.

[15] Equations (3) and (12)–(14) were solved simultaneously, using a numerical routine in Mathematica, for the

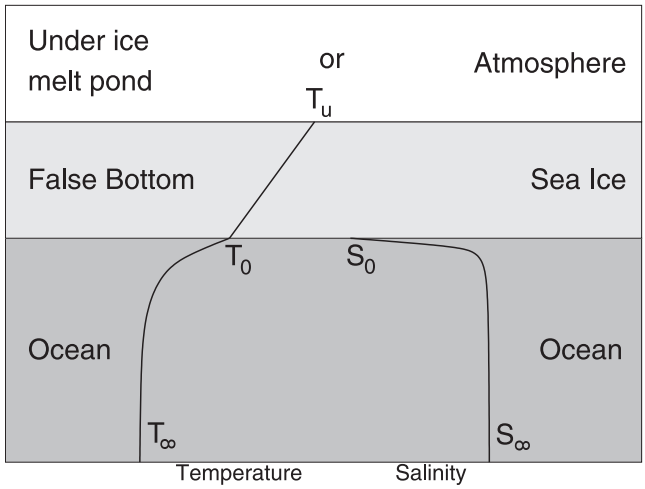

Figure 2. Sketch of the temperature and salinity profiles through the ice and ocean when purely diffusional processes occur. T_∞ and S_∞ are the far-field properties of the salt water, and T_0 and S_0 are the interface properties. For simplicity, the temperature profile in the ice is assumed to be linear, and salt fluxes within the ice are neglected. The left side of the figure is annotated for a false bottom, while the right side is annotated for a layer of sea ice.

unknowns λ, λ_u, T_0 and S_0. The physical constants are given in Table 1. For simplicity, we used $S_i = 0$ psu. The dependence of λ and λ_u on the far-field temperature T_∞ and the far-field salinity S_∞ is shown in Figure 3. The figure shows that both λ and λ_u are of order unity and vary little with changing far-field properties. As λ_u is always larger than λ the thickness of the false bottom increases with time. Note that $\lambda = 1$ corresponds to an ablation of about 1 cm in the first day. The salinity and temperature of the lower interface vary little with far field properties, being between 0.01 and 0.54 psu and -0.001 and -0.03 °C, respectively, for the far-field properties shown in Figure 3.

2.3. Implications for Sea Ice

[16] In general, the ablation of a two-phase, two-component material such as sea ice is made complicated by the fact that internal dissolution can occur in addition to ablation at the interface with the bulk-liquid region [e.g. *Feltham and Worster*, 2000]. However, in the case of multi-year ice, whose bulk salinity is significantly less than that of the ocean, ablation takes place predominantly at the interface, and the results of the analytical model presented above for a false bottom can be used to gain some insight into the processes involved. The main difference between the false-bottom case calculated above and the normal sea ice case is the absence of growth at the upper interface of the latter. However, the processes involved in the bottom ablation are the same for both cases, thus allowing for the transfer of the model results to the normal (low-salinity) sea-ice case.

[17] The model shows that the interface between the ice and the salt water is very fresh owing to the dissolving ice, which causes the temperature there to be above the freezing point temperature of the far field (see Figure 2). The low salinity of the lower interface is due to the fact that the water formed by the dissolving ice is fresh, and that the salt diffusivity is so low that the rate at which salt is transported into this newly formed water is very small. As the temperature at the interface must be at the liquidus, the interface can be warmer than the far field; thus heat flux out of the ocean can be slowed or reversed even when the mixed layer is well above freezing. Heat diffuses much faster than salt, so it is the salt flux, rather than the heat flux, which essentially determines the interface properties and thus the rate of bottom ablation of sea ice, a fact often neglected in sea-ice models. The importance of this rate limiting effect was emphasized by *McPhee et al.* [1987], who showed that it was much more significant than earlier models had predicted. This result was used, for example, in coupled ice–ocean models by *McPhee* [1987], *Mellor and Kantha* [1989], and *Holland and Jenkins* [1999].

[18] The importance of salt fluxes can be better understood by considering, for example, fresh ice floating on salt water, with both being at the same temperature between the freezing point of the water and 0 °C. The ice dissolves in the water, even though one might expect no phase change to occur if only the temperature field is taken into account. The temperature at the interface in this case will be below the temperature of both the ice and the water owing to the liquidus condition at the interface. As we have seen, this decrease in temperature is due to physical-chemical processes involved in the change of state. This process leads to bottom ablation rates of order a centimeter per day. Were the temperature of the salt water above 0 °C, melting would lead to ablation rates of order a decimeter per day, so the

Table 1. Physical Constants Used for the Model Calculation

Symbol	Value
L	333.5 kJ kg^{-1}
c_{pw}	4.185 kJ kg^{-1} K^{-1}
κ_w	$1.39 \cdot 10^{-7}$ m^2 s^{-1}
κ_i	$1.15 \cdot 10^{-6}$ m^2 s^{-1}
D	$6.8 \cdot 10^{-10}$ m^2 s^{-1}

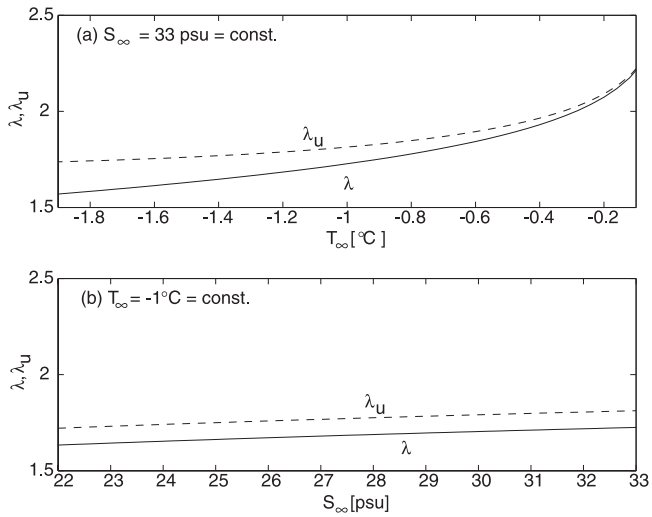

Figure 3. Scaled growth rates at the lower and upper interface, λ and λ_u, as functions of (a) far-field temperature T_∞ with $S_\infty = 33$ psu and (b) far-field salinity S_∞ with $T_\infty = -1$°C.

distinction between melting and dissolving is not purely academic.

3. Model of Bottom Ablation and False Bottom Evolution for Turbulent Conditions

3.1. Bottom Ablation of Sea Ice

[19] Because heat and salt fluxes in the ocean are strongly influenced by turbulence [see, e.g., *McPhee*, 1986, 1990; *McPhee et al.*, 1987], the model presented above was modified by replacing the molecular diffusive fluxes in the water with turbulent fluxes. The conservation relationships (1) and (2) are now written as

$$\rho L\dot{h} = k_i \left.\frac{\partial T}{\partial z}\right|_{\text{ice}} + \rho c_p \langle w'T' \rangle \tag{16}$$

$$(S_0 - S_i)\dot{h} = \langle w'S' \rangle, \tag{17}$$

where $\langle w'T' \rangle$ and $\langle w'S' \rangle$ are the Reynolds averaged turbulent heat and salt fluxes, respectively. Using dimensional analysis, these fluxes can be written as

$$\langle w'T' \rangle = -\alpha_h u_* (T_\infty - T_0) \tag{18}$$

$$\langle w'S' \rangle = -\alpha_s u_* (S_\infty - S_0), \tag{19}$$

where $u_* = (\langle u'w' \rangle^2 + \langle v'w' \rangle^2)^{1/4}$ is the friction velocity (u', v' w') is the fluctuation part of the velocity field, and α_h and α_s are turbulent exchange coefficients for heat and salt, respectively.

[20] The ratio of exchange coefficients α_h/α_s depends on the molecular diffusivities κ and D for heat and salt as well as on the roughness of the boundary. In general, good correlations have been found between experimental data and simple power laws of the form

$$\frac{\alpha_h}{\alpha_s} = \left(\frac{\kappa}{D}\right)^n,$$

[*McPhee et al.*, 1987]. It has been found that $2/3 < n < 0.8$ for hydraulically rough surfaces [*Owen and Thomson*, 1963; *Yaglom and Kader*, 1974]. For $D = 6.8 \cdot 10^{-10}$ m^2 s^{-1} and $\kappa = 1.39 \cdot 10^{-7}$ m^2 s^{-1}, this implies that

$$35 \le \frac{\alpha_h}{\alpha_s} \le 70. \tag{20}$$

McPhee et al. [1999] found, from measurements of turbulence intensity and heat transfer beneath sea ice, that a Stanton number,

$$St_* = \frac{\langle w'T' \rangle}{u_*[T_\infty - T_{\text{freeze}}(S_\infty)]}, \tag{21}$$

based on the departure of the mixed-layer temperature from its freezing point is approximately constant over a wide range of surface friction Reynolds numbers. Average values lay between 0.005 and 0.006. Although, as we have seen in the previous section, T_0 is above the freezing point of the far field and varies with the rate of salt transport, we have found that St_* as defined in equation (21) is predicted to be almost constant for thick ice, in agreement with the data collected and analyzed by *McPhee et al.* [1999], but not for thin ice (see below). Therefore, having chosen a value for α_h/α_s, we determined a value of α_h to give a value of St_* within the range given by *McPhee et al.* [1999] when $h = 2$ m. Having thus fixed the value of α_h based on measurements under thick ice, we can extend the model developed by *McPhee et al.* [1999] to make predictions also for thin ice, including the very thin ice characteristic of false bottoms.

[21] Combining equations (16)–(19) and rearranging terms leads in connection with equation (3) to a system of conditions at the interface for turbulent flow,

$$\dot{h}Q_L = \kappa_i \left.\frac{\partial T}{\partial z}\right|_{\text{ice}} + \alpha_h u_* (T_\infty - T_0) \tag{22}$$

$$\dot{h}(S_0 - S_i) = \alpha_s u_* (S_\infty - S_0), \tag{23}$$

where $Q_L = L/c_p$, sometimes being called kinematic latent heat with units K. The system is closed for a known heat flux from the ice. For example, the assumption of a linear temperature profile in the ice gives

$$\kappa_i \left.\frac{\partial T}{\partial z}\right|_{\text{ice}} = \kappa_i \frac{T_s - T_0}{h}, \tag{24}$$

where T_s is the surface temperature of the ice and h is the ice thickness. Using equations (3) and (22)–(24), it is possible to calculate $\dot{h}$, S_0 and T_0 in terms of far-field properties T_∞ and S_∞ by eliminating two of the unknowns to obtain a quadratic expression for the third one.

3.2. False Bottom Upper Surface Model

[22] The model just presented is valid for bottom ablation of both normal sea ice and false bottoms. The growth rate of the upper boundary of a false bottom can be calculated from the purely thermodynamic condition at the interface

$$\rho L_u \dot{h}_u = k_i \left.\frac{\partial T}{\partial z}\right|_{\text{ice}} - k_w \left.\frac{\partial T}{\partial z}\right|_{\text{freshwater}}, \tag{25}$$

which is the Stefan condition (equation (1)) for the upper surface of the false bottom. Here $L_u = L_0(1 - \sigma)$ is the latent heat of fusion, adjusted for the frazil ice fraction σ in the fresh water melt pond. The first term on the right-hand side describes the conductive heat flux in the false bottom just below the upper boundary, whereas the second term describes the heat flux from the fresh water in the cavity to the top of the false bottom. To calculate the latter, we set up a radiation model, using the simplified scheme presented by *Grenfell and Maykut* [1977]. We used an extinction coefficient of 0.044 m^{-1} for fresh water, which leads to negligible radiative heating. Owing to frazil ice crystals floating in the water in the cavity, the extinction coefficient might be much higher but, with the presence of frazil ice, all the absorbed solar energy would go into melting of the frazil, keeping the temperature of the water in the cavity at 0°C without affecting the surrounding ice walls and the

false bottom. Combining these arguments, the neglect of heat flux from the fresh water that led to equation (6) is reasonable, as both the water and the upper boundary of the false bottom will have a temperature of 0°C.

4. Model Results

4.1. Model Results for a Laboratory Experiment

[23] To test the model for the idealized diffusive case, governed by equations (1)–(5), we simulated the experiment of *Martin and Kauffman* [1974]. In their experiment, fresh water at 0°C was put on top of salt water with a salinity of 34 psu at its freezing point, in order to simulate the growth of a false bottom. As the model presented above does not take salt transport through the false bottom into account, we started the model run with an initially solid ice layer, as formed on day 15 in the experiment, and let the model run until day 35 of the experiment. For this simulation we used again the values given in Table 1 and $S_i = 0$ psu.

[24] To keep the salt water at its freezing point, *Martin and Kauffman* [1974] let it recirculate through a reservoir of salt water, which was kept at the freezing point. To simulate this in the model, we applied Newtonian cooling to the salt water layer by adding the source term $\gamma(T - T_\infty)$ to equation (5), with $\gamma = 1/7200\ \mathrm{s}^{-1}$ and $T_\infty = -1.8$°C, according to the experimental set up. The result of the model run and the data from the experiment are shown in Figure 4. The measured and predicted evolution of the ice sheet are given after day 15, when a solid ice sheet was formed in the tank. The model result fits the measurements very well when we start with a 5-cm layer of ice on day 15. At the beginning of the sequence the measured thickness is larger than the simulated one, because Martin and Kauffman measured the maximum thickness of an initially irregular ice sheet. The agreement between the model and the experiment is therefore better for the time period after day 21 when the bottom of the ice became smooth in the experiment.

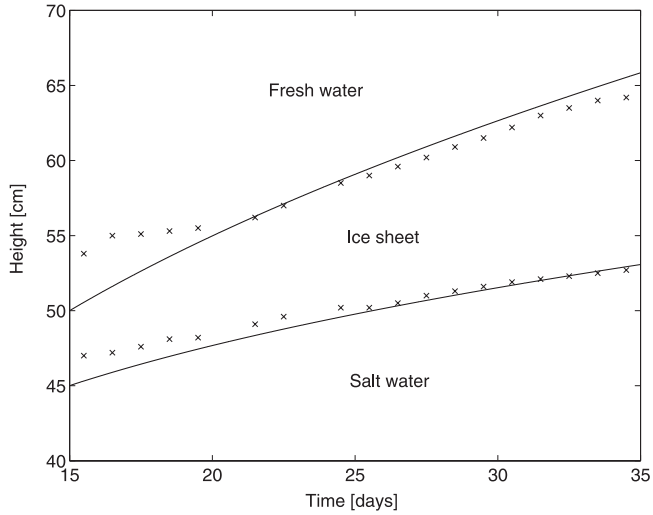

Figure 4. Comparison of model results and experimental data from *Martin and Kauffman* [1974]. The solid lines show the model results for the upper and lower ice boundary, and the crosses are the data measured in the experiment. The *x*-axis shows the day of the measurements, and the *y*-axis shows height above the bottom of the experimental tank.

4.2. Sensitivity of the Model Results for Turbulent Conditions

[25] Using the turbulent model governed by equations (3) and (22)–(24), we calculated how the interface properties and ablation rates depend on ice thickness and friction velocities. The results are shown in Figure 5. Figure 5a shows the dependence of interface temperature and ablation rate for different friction velocities, with far-field properties being $T_\infty = -1.6$ °C, $S_\infty = 34$ psu and ice thickness 0.5 m. For the purposes of this illustration, we have taken $\alpha_h/\alpha_s = 35$, which produces $\alpha_h = 0.0095$ according to the procedure described above. For simplicity, the ice was assumed to have a linear temperature profile with the surface being at 0°C. The interface temperature T_0 decreases for increasing friction velocities, being below the far-field temperature for $u_* > 0.002\ \mathrm{m\ s}^{-1}$. This is due to the fact that, for higher friction velocities, more salt is transported to the interface, leading to a higher salinity and thus a lower liquidus temperature at the interface. It is important to note that the interface temperature is directly related neither to the far-field temperature nor to the freezing temperature of the far field. Rather it is dictated by the rate of salt transfer to the interface.

[26] Figure 5b shows the dependence of the interface temperature and ablation rates on ice thickness. Far-field properties are as above with $u_* = 0.005\ \mathrm{m\ s}^{-1}$. The temperature profile in the ice is again linear with the surface being at 0°C. The temperature at the interface is higher for thin ice than for thick ice, which, in connection with the constant salt flux resulting from the constant friction velocity, leads to increased bottom ablation. The model of *McPhee* [1992], in which the heat flux from the ocean is expressed as

$$H_w = \rho c_p St_* u_* [T_\infty - T_{\mathrm{freeze}}(S_\infty)], \tag{26}$$

with $St_* = 0.006$, predicts similar ablation rates to those shown in Figure 5a for 0.5-m-thick ice and a constant ablation rate of 0.7 cm day^{-1} for the conditions of Figure 5b. We see that the present model predicts significantly larger ablation rates for thin ice. The heat flux given by equation (26) is an appropriate scheme during freezing, since the ice platelets that make up sea ice extend to engulf any salinity boundary layer and the interface temperature is very close to the freezing temperature of the far field [*Worster*, 2000]. However, our results here suggest that equation (26) should not generally be used in cases of ablation. For ice thicker than 1 m, using equation (26) gives ablation rates about 10% lower than the ones obtained by our model for most of the parameter space of interest during summer. For ice thinner than 0.5 m the deviations are larger than 20% for most of the parameter space.

[27] The only parameters in the model that are difficult to obtain independently from direct field measurements are the turbulent transfer coefficients for heat α_h and salt α_s. As shown in Figure 6, the calculated ablation rates vary by about 20% for a reasonable range of these coefficients. The figure shows the variation of bottom ablation rates with

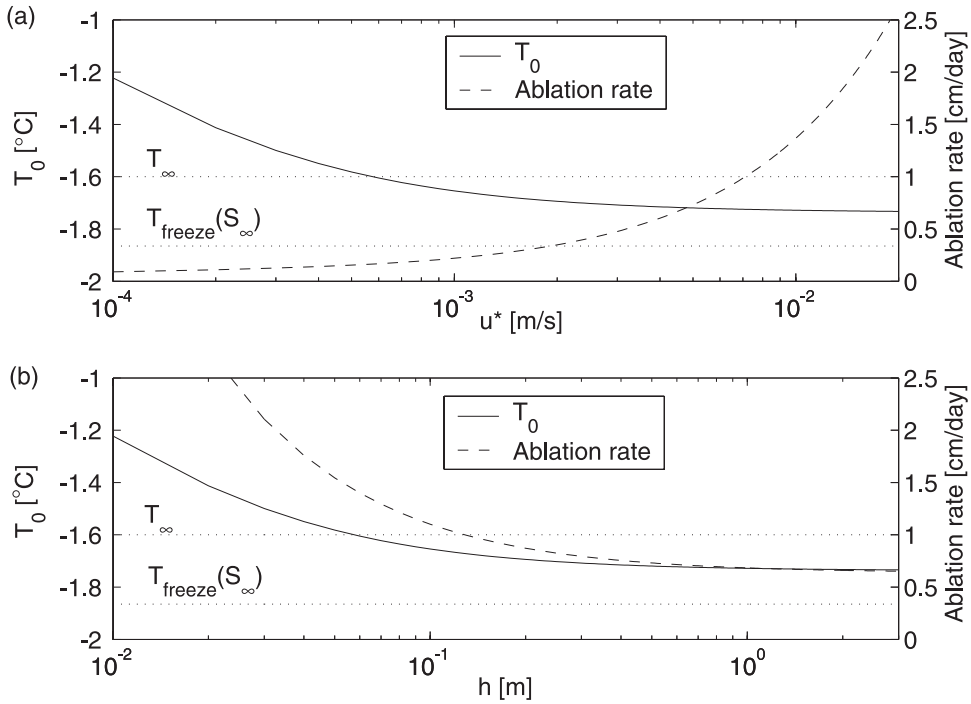

Figure 5. (a) Interface temperature (axis to the left) and bottom ablation rate (axis to the right) for varying friction velocity u_* with $T_\infty = -1.6$ °C, $S_\infty = 34$ psu, ice thickness $h_i = 0.5$ m, $\alpha_h = 0.0095$, and $\alpha_h/\alpha_s = 35$. The dotted horizontal lines mark the far-field temperature T_∞ and the far-field freezing point $T_{\text{freeze}}(S_\infty)$. (b) As in Figure 5a, but for varying ice thickness with constant friction velocity $u_* = 0.005$ m s^{-1}.

different model input parameters. Each parameter was varied from its lower to its upper value indicated at the ends of the respective bar. All the other parameters were kept at the value indicated by the line through the middle of the figure. The resulting maximum and minimum ablation rates are represented by the ends of the respective bar. All directly measurable properties (friction velocity u_*, far-field salinity S_∞ and temperature T_∞, ice salinity S_i and ice thickness h_i) were varied according to values typical for the Arctic summer. The ratio α_h/α_s was varied between the values calculated in equation (20), and α_h was chosen in each case to give $St_* = 0.0055$ at $h = 1$ m.

[28] As can be seen from Figure 6 the far-field properties have a very strong influence on the calculated ablation rates, whereas these rates only vary by about 20% for different values of α_h and α_s. Even though the derived variabilities are only valid for the particular choice of values consistent with the AIDJEX data and the sensitivity might look different for a different set of parameters (due to the nonlinearity of the model), it can be seen that the variability of the calculated ablation rates with differing α_h and α_s allows values for α_h to be obtained from field measurements given a value of α_h/α_s appropriate to the roughness of the ice.

4.3. Model Results for AIDJEX and SHEBA Data

[29] To illustrate the model and its predictions for oceanographic conditions, we use data from both the AIDJEX and the SHEBA field experiments. Beginning in March 1975, the Arctic Ice Dynamics Joint Experiment (AIDJEX) maintained for more than a year several manned drift stations in the central Arctic. Among a wide variety of measurements (see *Pritchard* [1980] for details), ice-thickness measurements were performed every second day. Figure 7 shows ice thicknesses at different locations near the AIDJEX-station Big Bear for the time period Jun 10, 1975 (day 160) until September 17, 1975 (day 260). The thicknesses were measured against a reference stick which was fixed in the

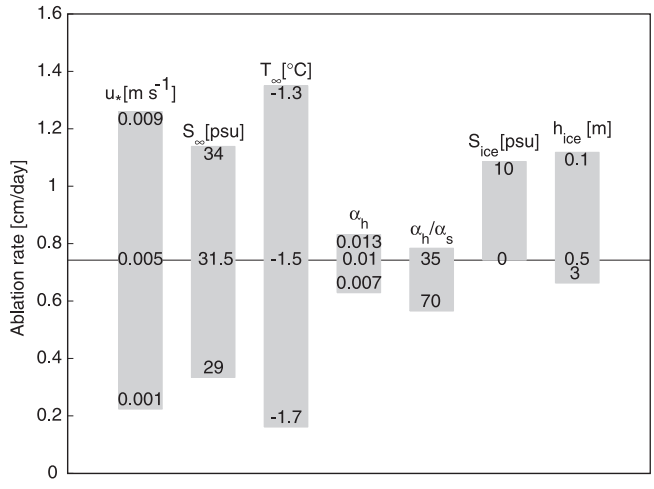

Figure 6. Dependence of ablation rates on model parameters. For each of the input parameters indicated at the bars this parameter was varied from its lower to its upper value, indicated at the ends of the bar. The values of the other parameters were kept constant at the values indicated along the line in the figure. The position of the upper and lower end of the bar indicates the ablation rate (y-axis).

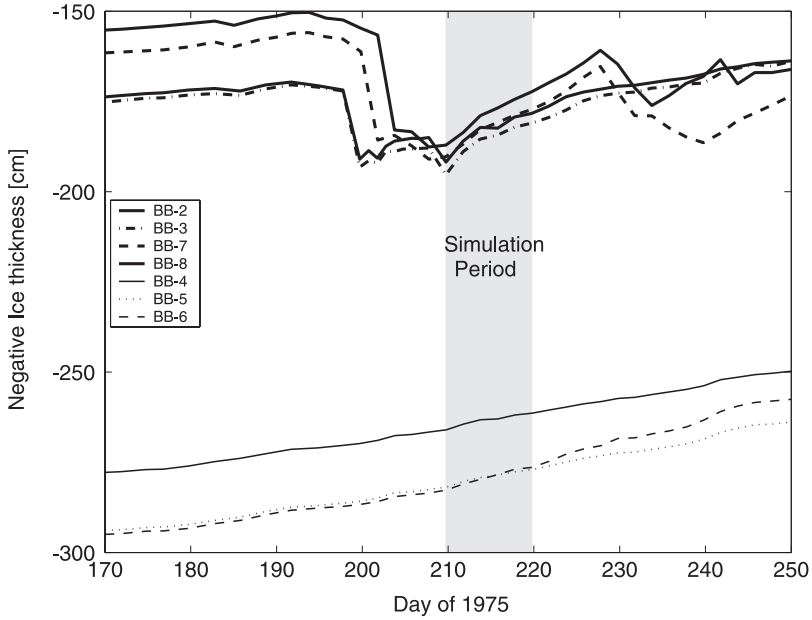

Figure 7. Ice thicknesses (negative numbers) as measured during the 1975 AIDJEX Project in the Beaufort Gyre. All thickness changes are due to bottom ablation and accretion. Note the steady decrease in thickness for thick ice (gauges BB-4, BB-5, BB-6) compared to an increase in thickness for initially thin ice (gauges BB-2, BB-3, BB-7, BB-8).

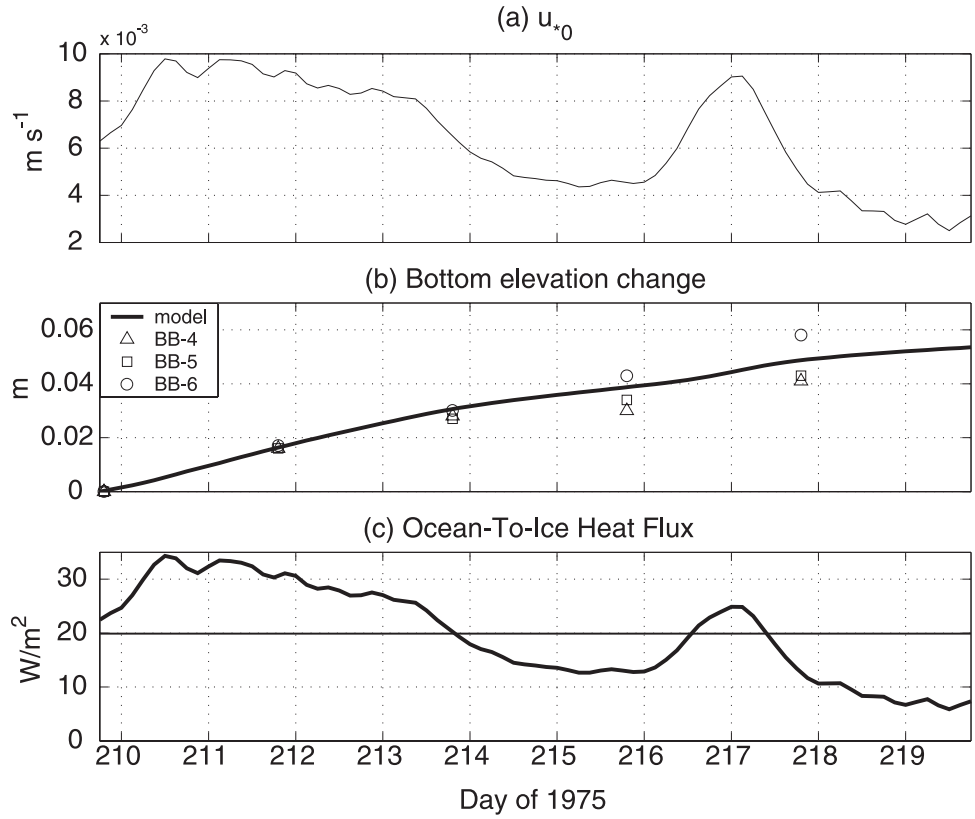

Figure 8. (a) Friction velocity during AIDJEX as calculated from Rossby-number similarity theory with a friction length $z_0 = 0.006$ m. See text for details on the far-field temperature and salinity. (b) Simulated and measured ablation for deep thickness gauges (2.5 m to 3 m) with no false bottom formation during AIDJEX. Model parameters: $\alpha_h = 0.0095$, $\alpha_h/\alpha_s = 35$. (c) Heat flux from the ocean to the ice at the ice-ocean interface. The horizontal line shows the average heat flux, which is around 18 W m^{-2} upward.

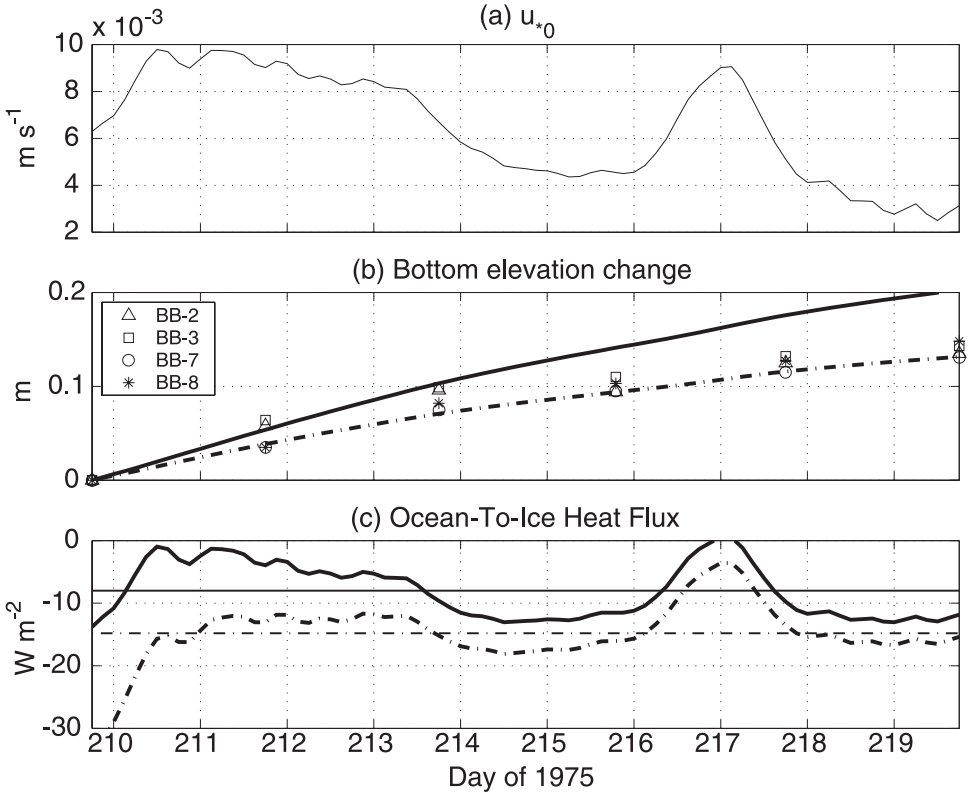

Figure 9. (a) Same as Figure 8a. (b) Simulated and measured ablation for shallow thickness gauges (1.5 m to 2 m) with false bottom formation during AIDJEX. Model parameters: solid line: $\alpha_h = 0.0095$, $\alpha_h/\alpha_s = 35$, dash-dotted line: $\alpha_h = 0.0135$, $\alpha_h/\alpha_s = 70$. (c) Heat flux from the ocean to the ice at the ice-ocean interface. The horizontal lines show the average heat fluxes for the two sets of model parameters. The average heat fluxes are around 8 to 15 W m^{-2} downward.

ice, so all thickness changes in Figure 7 are due to bottom processes. Whereas the ice thickness decreases steadily for thick ice (gauges BB-4, BB-5, BB-6), the time series of the thin ice shows periods with rapidly increasing thickness. The rapid increase in thickness around day 200 is due to flushing of surface melt water through an artificial bore hole and the creation of a false bottom. The thickness is measured to the base of this false bottom. As shown by *Eicken et al.* [2002], even without the drillings a significant part of the surface meltwater would have been transported under the ice through cracks and leads, leading to the formation of false bottoms. There is evidence of the formation of a false bottom beneath the thinner ice around day 210 as well. We have modeled the bottom ablation of the thick ice and the evolution of this second false bottom for 10 days starting from day 209.75, as indicated in Figure 7.

[30] Because of lack of temperature and salinity data for that specific time period, we used linearly interpolated data for the far-field properties. These data give a decrease of temperature from -1.47°C at day 209.75 to -1.52°C at day 219.75 and a slight increase of salinity from 29.84 psu to 29.85 psu for the same period. The friction velocity was calculated from Rossby-number similarity [see, e.g., *McPhee*, 1990] with a roughness length $z_0 = 0.6$ cm, chosen to coincide with the value obtained by *McPhee* [2002] for the undeformed SHEBA floe. The model predictions for the thick ice are shown in Figure 8, where the ablation is well simulated. The results are insensitive to the values chosen for α_h/α_s: The predicted ablation rates differ only about 1% for the range give in equation (20).

[31] The model predicts that the heat flux between the ice and the ocean was upward beneath the thick ice, i.e., that the ice-ocean interface had a temperature below the far-field ocean temperature. The ocean is predicted to have supplied an average heat flux of around 18 W m^{-2} to the ice, as shown in Figure 8b, though there is no direct verification of this.

[32] In Figure 9b we show our predictions for the evolution of the false bottom beneath the thinner ice. There is an additional fitting parameter in this case, namely the ''initial'' thickness of the false bottom, which we chose to be 2.5 cm at day 209.75. The prediction using $\alpha_h/\alpha_s = 70$ (appropriate to a rough boundary) fits the data better than that using $\alpha_h/\alpha_s = 35$. It is significant, however, that the uncertainty in the prediction arising from the uncertainty in α_h/α_s is much less than the difference in the ablation rates for thin and thick ice shown in Figures 8b and 9b. The bottom ablation of the false bottom is well predicted at all four gauges, as shown in Figure 9b. Note that the absolute values of the bottom elevation change are 2.5 to 3 times the change in thickness of the thick ice. This is due to the larger heat flux through the thin ice of the false bottom. As shown in Figure 9c, the model predicts that the ice-ocean heat flux was directed downward beneath the false bottom, with an average value of -8 to -15 W m^{-2}.

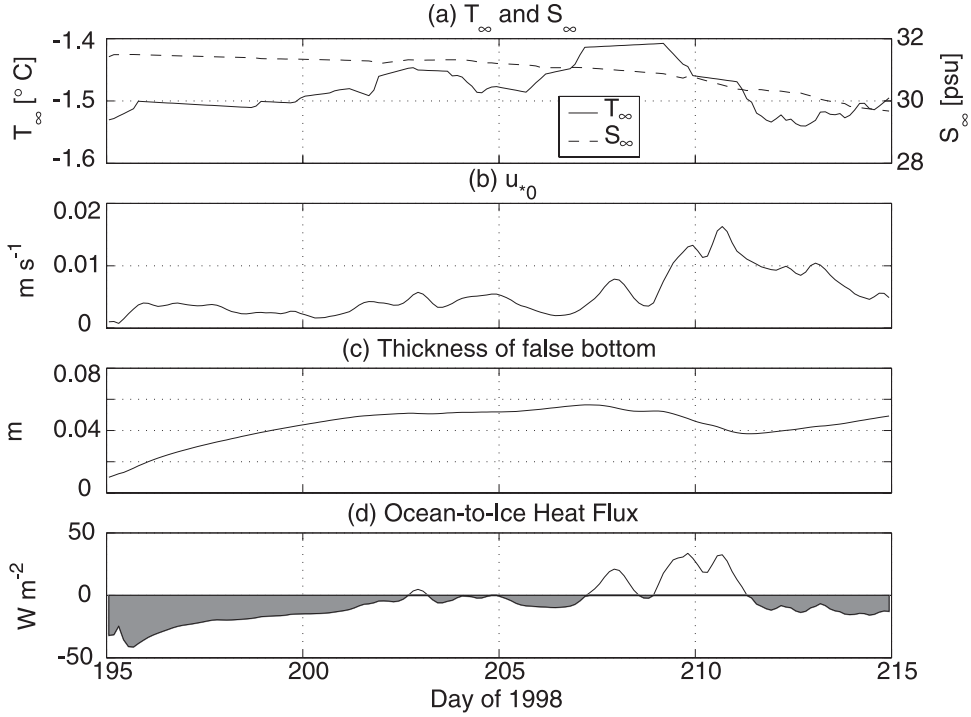

Figure 10. (a) Far-field temperature and salinity from SHEBA data during summer 1998. (b) Friction velocity u_* for a roughness length $z_0 = 0.006$ m. (c) Simulated evolution of the thickness of a false bottom formed at day 195. Model parameters: $\alpha_h = 0.0095$, $\alpha_h/\alpha_s = 35$. (d) Ocean heat flux at the base of the false bottom (positive is from the water to the ice).

[33] In both the cases of thick and thin ice at AIDJEX, the bottom ablation is a result of dissolution, not melting; the flux of salt from the ocean was a necessary ingredient effecting phase change, since the ocean temperature was below the melting temperature of the ice based on its bulk salinity. The temperature of the ice-ocean interface is determined by the coupled interactions of heat and salt transport and, as we have seen, can be either less or greater than the ocean temperature. Although in a formal asymptotic sense (in the limit of small diffusivity ratio D/κ) the ablation rate is limited by salt transport, the parameter values associated with sea ice, particularly the large value of the Stefan number $S = L/c_p\Delta T \approx 80$, result in heat transport and salt transport playing roles of comparable magnitude in determining the ablation rate.

[34] We have also used our model to make (uncorroborated) predictions of some important variables associated with the 1998 SHEBA camp. In particular, we have determined some interesting predictions of the consequences of a storm that passed through the camp. The data utilized and the predictions made are shown in Figure 10. The far-field temperature and salinity are shown in Figure 10a. While there is no obvious trend in the temperature field, the salinity decreased steadily during the whole period. The values of u_* inferred from measurements of the current velocity 1 m below the ice (see *McPhee* [2002] for details) and using a value of $z_0 = 0.6$ cm are shown in Figure 10b. There was a period of relative calm between day 195 and day 207, in which surface meltwater could have collected under the ice, leading to the formation and growth of false bottoms and an increase in ice thickness at various locations. At the SHEBA site, this period corresponded to the second major period of false-bottom formation observed both through direct sampling [*Eicken et al.*, 2002] and through indirect measurements at the mass-balance gauges [*Perovich et al.*, 2003]. Nonsystematic, anecdotal observations also indicate that the warming and salinization of the uppermost water layers and the disintegration of the ice cover in the aftermath of the storm resulted in melting and disintegration of false bottoms in the early days of August. Subsequently, some renewed false-bottom formation was found at one site around day 220, close to the end of the field experiment.

[35] Figure 10c shows the simulated evolution of a false bottom initiated at day 195 with a thickness of 1 cm. Using the same value of z_0 as before and taking $\alpha_h/\alpha_s = 35$, we predict a steady increase in the thickness of the false bottom until day 207, when it is almost 6 cm thick. At that time the storm came through, which increased the inferred value of u_* substantially, as shown in Figure 10b. In consequence, the salt flux from the ocean to the ice is predicted to have increased, leading to a rapid ablation of the false bottom by about 2 cm to a little less than 4 cm in about 4 days. Given the assumptions of our simple model, particularly the neglect of radiative heat transfer and of any salt within the melt pond and false bottoms, it is impossible for the false bottom to disappear entirely by ablation alone. However, the enhanced ablation caused by the storm is likely to have enhanced the mechanical break up of many of the false bottoms observed during the storm. This storm-induced break up of false bottoms can cause a sudden input of fresh water to the underlying ocean, as the melt water in the under-ice cavity is mixed down by the enhanced turbulence.

[36] Figure 10d shows that the ocean-ice heat flux is predicted to have been directed toward the ocean during the quiescent period but toward the ice during the storm. The lowering of the ice-ocean interface temperature caused by the enhanced salt flux during the storm is predicted to have been sufficient to lower the temperature below the ocean temperature and allow the heat of the ocean to assist in the ablation of the false bottom.

5. Conclusions

[37] In this paper, we have focused attention on the role of salt transport effecting the ablation of sea ice, and assessed the role of false bottoms formed beneath under-ice melt ponds. A self-similar model of the simultaneous, diffusion-controlled growth and ablation of a false bottom was developed and solved. The analytical solution highlights the controlling influence of salt transport by showing that the thickness of the false bottom and the amount of ablation it suffers both scale with $\sqrt{Dt}$, where D is the diffusivity of salt in water. The simple model was extended to take account of turbulent heat and salt transport characteristic of the oceanic system. The model is able to simulate both the bottom ablation of normal sea ice and the evolution of false bottoms. As input data, only knowledge of the far-field temperature and salinity and the friction velocity at the ice-ocean interface is necessary. The predictions of the model compare well with field data from the AIDJEX. We have additionally applied the model to make predictions based on data collected during the 1998 SHEBA camp. The model suggests that significant thickening and migration of false bottoms should have occurred during periods of quiet weather but that significant thinning of false bottoms should have occurred during a storm that passed by on day 210 of 1998.

[38] An important implication of the model is that the ice-ocean-interface temperature is dictated in large part by the rates of salt transport, and can be either higher or lower than the ocean temperature depending on circumstances. In consequence, the ice-ocean heat flux can be directed either toward the ocean or toward the ice. A major implication of this study is therefore that proper account must be made of salt transport in coupled ice-ocean models even to make appropriate estimates of heat budgets. Parameterizations of bottom ablation neglecting the salt flux and assuming the bottom of the melting sea ice to be at the freezing point of the far field may lead to an underestimate of ablation rates of up to 1 order of magnitude for ice thinner than 10 cm and to still significant errors for thicker ice (see Figure 5). For ice thicker than 1 m the simple parameterization of *McPhee* [1992] can be used without large deviations from our model.

[39] The model results suggest that it is potentially important to understand and to measure the extent and distribution of under-ice melt ponds and false bottoms. During periods of thickening false bottoms, there is a significant heat flux into the mixed layer of order 10 W m^{-2}, comparable to other heat fluxes such as solar radiation divergence and the upward ocean heat flux from depth. The heat flux into the mixed layer appears locally under a false bottom but the resulting increase in mixed-layer temperature will have regional consequences for the development of the overall ice pack.

[40] The thickening of thin ice by false-bottom formation leads to longer-lasting sea ice and thus smaller ice-free areas, which might be an important mechanism affecting the surface albedo. The simultaneous bottom ablation of thick ice and false bottom formation causes a leveling of the under-ice topography that could be important for the modeling of sea-ice dynamics. Furthermore, both the slow fresh water input owing to ablation of false bottoms and the rapid input of fresh water when false bottoms break up in storms are important in terms of the overall stability and salinity of the mixed layer, particularly toward the end of the melting season, when the direct input of surface meltwater (that earlier dominated the fresh water fluxes to the ocean) ceases. The predicted migration rates of false bottoms are sensitive to the values chosen for α_h and α_s, so accurate measurements of migration rates and heat fluxes in comparison with predictions will constrain the values of these parameters and lead to better parameterization of turbulent fluxes under ice in general.

[41] **Acknowledgments.** We would like to thank John Wettlaufer for interesting discussions and helpful comments on the paper. D. N. and M. G. W. are very grateful for the hospitality and supportive environment of the Applied Physics Laboratory of the University of Washington, where they were both visitors while much of this work was done. We thank the reviewers for their constructive comments. This research was made possible by support from the National Science Foundation, Office of Polar Program under grants OPP-0084269, OPP0084271, and OP0084275, from the Office of Naval Research under contract N00014-96-C-0032 and from the Studienstiftung des Deutschen Volkes.

References

Abramovitz, M., and I. A. Stegun, *Handbook of Mathematical Functions*, Dover, New York, 1965.

Andreas, E. L., and S. F. Ackley, On the differences in ablation seasons of the Arctic and Antarctic sea ice, *J. Atmos. Sci.*, *39*, 440–447, 1982.

Carslaw, H. S., and J. C. Jaeger, *Conduction of Heat in Solids*, Oxford Univ. Press, New York, 1986.

Cherepanov, N. V., I. L. Nazintsev, and K. P. Tyshko, Contact supercooling of water layers and bottom ice formation in the sea (in Russian), in *Electro Physical and Physical-Mechanical Properties of Ice*, edited by V. V. Bogordskii and V. P. Gavrilo, pp. 124–134, Gidrometeoizdat, St. Petersburg, Russia, 1989.

Eicken, H., Structure of under-ice melt ponds in the central Arctic and their effect on the sea-ice cover, *Limnol. Oceanogr.*, *39*(3), 682–694, 1994.

Eicken, H., H. R. Krouse, D. Kadko, and D. K. Perovich, Tracer studies of pathways and rates of meltwater transport through Arctic summer sea ice, *J. Geophys. Res.*, *107*(C10), 8046, doi:10.1029/2000JC000583, 2002.

Feltham, D. L., and M. G. Worster, Similarity solutions describing the melting of a mushy layer, *J. Cryst. Growth*, *208*, 746–756, 2000.

Gradinger, R., Occurrence of an algal bloom under Arctic pack ice, *Mar. Ecol. Prog. Ser.*, *131*, 301–305, 1996.

Grenfell, T. C., and G. A. Maykut, The optical properties of ice and snow in the Arctic Basin, *J. Glaciol.*, *18*, 445–463, 1977.

Hanson, A. M., Studies of the mass budget of Arctic pack-ice floes, *J. Glaciol.*, *5*, 701–709, 1965.

Holland, D. M., and A. Jenkins, Modeling thermodynamic ice-ocean interactions at the base of an ice shelf, *J. Phys. Oceanogr.*, *29*, 1787–1800, 1999.

Jeffries, M. O., K. Schwartz, K. Morris, A. D. Veazey, H. R. Krouse, and S. Cushing, Evidence for platelet ice accretion in Arctic sea ice development, *J. Geophys. Res.*, *100*(C6), 10,905–10,914, 1995.

Martin, S., and P. Kauffman, The evolution of under-ice melt ponds, or double diffusion at the freezing point, *J. Fluid. Mech.*, *64*, 507–527, 1974.

Maykut, G. A., An introduction to ice in the polar oceans, *APL-UW 8510*, Univ. of Wash., Seattle, Wash., 1985.

McPhee, M. G., The upper ocean, in *The Geophysics of Sea Ice*, edited by N. Untersteiner, pp. 133–141, Plenum, New York, 1986.

McPhee, M. G., A time-dependent model for turbulent transfer in a stratified oceanic boundary layer under pack ice, *J. Geophys. Res.*, *92*(C7), 6977–6986, 1987.

McPhee, M. G., Small scale processes, in *Polar Oceanography, Part A: Physical Science*, pp. 287–334, Academic, San Diego, Calif., 1990.

McPhee, M. G., Turbulent heat flux in the upper ocean under sea ice, *J. Geophy. Res.*, *97*(C4), 5365–5379, 1992.

McPhee, M. G., Turbulent stress at the ice/ocean interface and bottom surface hydraulic roughness during the SHEBA drift, *J. Geophy. Res.*, *107*(C10), 8037, doi:10.1029/2000JC000633, 2002.

McPhee, M. G., G. A. Maykut, and J. H. Morison, Dynamics and thermodynamics of the ice/upper ocean system in the marginal ice zone of the Greenland sea, *J. Geophys. Res.*, *92*(C7), 7017–7031, 1987.

McPhee, M. G., C. Kottmeier, and J. H. Morison, Ocean heat flux in the central Weddell Sea in winter, *J. Phys. Oceanogr.*, *29*, 1166–1179, 1999.

Mellor, G. L., and L. H. Kantha, An ice-ocean coupled model, *J. Geophys. Res.*, *94*(C4), 10,937–10,954, 1989.

Nansen, F., *Farthest North*, Constable, Westminster, England, 1897.

Notz, D., Prozesse der Meereisentwicklung in der sommerlichen Arktis, Diploma thesis, Meteorol. Inst., Univ. Hamburg, Hamburg, Germany, 2001.

Owen, P. R., and W. R. Thomson, Heat transfer across rough surfaces, *J. Fluid. Mech.*, *15*, 321–334, 1963.

Perovich, D. K., et al., Year on ice gives climate insights, *Eos. Trans. AGU*, *80*, 481, 485–486, 1999.

Perovich, D. K., T. C. Grenfell, J. A. Richter-Menge, B. Light, W. B. Tucker III, and H. Eicken, Thin and thinner: Ice mass balance measurements during SHEBA, *J. Geophys. Res.*, *108*(C3), 8050, doi:10.1029/2001JC001079, 2003.

Pritchard, R. S., (Ed.), *Sea Ice Processes and Models*, Univ. of Wash. Press, Seattle, Wash., 1980.

Untersteiner, N., Natural desalination and equilibrium salinity profile of perennial sea ice, *J. Geophys. Res.*, *73*(4), 1251–1257, 1968.

Untersteiner, N., and F. I. Badgley, Preliminary results of thermal budget studies on Arctic pack ice during summer and autumn, in *Arctic Sea Ice*, *Publ. 598*, pp. 85–92, Natl. Acad. of Sci., Natl. Res. Counc., Washington, D.C., 1958.

Wadhams, P., and S. Martin, Processes determining the bottom topography of multiyear Arctic sea ice, in *Sea Ice Properties and Processes*, edited by W. F. Weeks and S. F. Ackley, pp. 136–141, Monogr. 90-1, Cold Regions Res. and Eng. Lab., Hanover, N. H., 1990.

Woods, A. W., Melting and dissolving, *J. Fluid Mech.*, *239*, 429–448, 1992.

Worster, G., Solidification of fluids, in *Perspectives in Fluid Dynamics*, edited by G. K. Batchelor, H. K. Moffatt, and M. G. Worster, pp. 393–446, Cambridge Univ. Press, New York, 2000.

Yaglom, A. M., and B. A. Kader, Heat and mass transfer between a rough wall and turbulent flow at high Reynolds and Peclet numbers, *J. Fluid Mech.*, *62*, 601–623, 1974.

H. Eicken, Geophysical Institute, University of Alaska, 903 Koyukuk Drive, P.O. Box 757320, Fairbanks, AK 99775, USA. (hajo.eicken@gi.alaska.edu)

G. A. Maykut, Department of Atmospheric Sciences, University of Washington, Seattle, WA 98195, USA. (maykut@atmos.washington.edu)

M. G. McPhee, McPhee Research Company, 450 Clover Springs Road, Naches, WA 98937, USA. (mmcphee@starband.net)

D. Notz and M. G. Worster, Institute of Theoretical Geophysics, Department of Applied Mathematics and Theoretical Physics, University of Cambridge, Wilberforce Road, Cambridge CB3 0WA, UK. (dn240@cam.ac.uk; grae@esc.cam.ac.uk)

K. H. Schlünzen, Meteorologisches Institut, Zentrum für Meeres- und Klimaforschung, Universität Hamburg, Bundesstraße 55, 20146 Hamburg, Germany. (schluenzen@dkrz.de)